Adaptive Real-Time Bioheat Transfer Models for Computer-Driven MR-Guided Laser Induced Thermal Therapy

David Fuentes, Yusheng Feng, Andrew Elliott, Anil Shetty, Roger J. McNichols, J. Tinsley Oden, and R. J. Stafford*

***Abstract*—The treatment times of laser induced thermal therapies (LITT) guided by computational prediction are determined by the convergence behavior of partial differential equation (PDE)-constrained optimization problems. In this paper, we investigate the convergence behavior of a bioheat transfer constrained calibration problem to assess the feasibility of applying to real-time patient specific data. The calibration techniques utilize multiplanar thermal images obtained from the nondestructive *in vivo* heating of canine prostate. The calibration techniques attempt to adaptively recover the biothermal heterogeneities within the tissue on a patient-specific level and results in a formidable PDE constrained optimization problem to be solved in real time. A comprehensive calibration study is performed with both homogeneous and spatially heterogeneous biothermal model parameters with and without constitutive nonlinearities. Initial results presented here indicate that the calibration problems involving the inverse solution of thousands of model parameters can converge to a solution within three minutes and decrease the $\|\cdot\|^2_{L_2(0,T;L_2(\Omega))}$ norm of the difference between computational prediction and the measured temperature values to a patient-specific regime.**

***Index Terms*—Magnetic resonance (MR) temperature imaging, PDE-constrained optimization, real-time computing.**

I. Introduction

THE FEASIBILITY of developing an adaptive feedback control system which uses dynamic multiplanar magnetic resonance imaging (MRI) temperature measurements to adaptively conform delivery of therapy to the prescribed treatment plan in real-time during MR-guided laser induced thermal therapy has been demonstrated [9]. The cyberinfrastructure [1], [6] inherent to the control system relies critically on the precise real-time orchestration of large-scale parallel computing, high-speed data transfer, a diode laser, dynamic imaging, visualizations, inverse-analysis algorithms, registration, and mesh generation. We demonstrated that this integrated technology has significant potential to facilitate a reliable minimally invasive treatment modality that delivers a precise, predictable and controllable thermal dose prescribed by oncologists and surgeons. However, MR-guided LITT (MRgLITT) has just recently entered into patient use [4] and substantial translational research and validation is needed to fully realize the potential of this technology [18], [21] within a clinical setting. The natural progression of the computer-driven MRgLITT technology will begin with prospective pretreatment planning. Future innovations on the delivery side will likely involve combining robotic manipulation of fiber location within the applicator as well as multiple treatment applicators firing simultaneously.

Currently, the workflow of our treatment protocols are divided into data acquisition, computational, and delivery phases. This paper focuses on the computational aspects of model calibration. A schematic of the procedure setup and workflow is provided in Figs. 1 and 2, respectively. Heterogeneous model calibration involving thousands of model parameters have been shown to deliver model predictions of unprecedented accuracy [7]. The goal of this study is to evaluate the feasibility of real-time patient specific heterogeneous model calibration for both linear and nonlinear constitutive models. Such calibrations are critical for maintaining the predictive power of the simulation during therapy and therefore in maximizing the efficiency of the therapy control loop. We briefly review the governing PDE-constrained optimization equations, present our results, and discuss the higher level implications for real-time control of MR-guided LITT as well as milestones within the translational research.

Manuscript received March 10, 2009; revised September 18, 2009. First published February 5, 2010; current version published April 21, 2010. This work was supported in part by National Institutes of Health under Grant 5T32CA119930-03 and Grant K25CA116291 and by the National Science Foundation under Grant CNS-0540033. *Asterisk indicates corresponding author.*

D. Fuentes, A. Elliott, and A. Shetty are with the Department of Imaging Physics, The University of Texas M.D. Anderson Cancer Center, Houston, TX 77030 USA (e-mail: dtfuentes@mdanderson.org; andrew.elliott@mdanderson.org; anil.shetty@mdanderson.org).

Y. Feng is with the Computational Bioengineering and Nanotechnology Laboratory, The University of Texas, San Antonio, TX 78749 USA (e-mail: yusheng.feng@utsa.edu).

R. J. McNichols is with BioTex, Inc., Houston, TX 77054 USA (e-mail: roger@biotexmedical.com).

J. Tinsley Oden is with the Institute for Computational Engineering and Sciences, The University of Texas, Austin TX 78712 USA (e-mail: oden@ices.utexas.edu).

*R. J. Stafford is with Department of Imaging Physics, The University of Texas M.D. Anderson Cancer Center, Houston, TX 77030 USA (e-mail: jstafford@mdanderson.org).

Color versions of one or more of the figures in this paper are available online at http://ieeexplore.ieee.org.

Digital Object Identifier 10.1109/TBME.2009.2037733

II. Calibration Problem

The problem of bioheat transfer model calibration is to determine the set of thermal parameters that minimize the $L_2(0,T;L_2(\Omega))$ norm of the difference between the predicted temperature field, $u(\mathbf{x},t)$ and the temperature field observed *in vivo* thermal images of the experiment $u^{\mathrm{MRTI}}(\mathbf{x},t)$. In our experiments, the MR temperature imaging (MRTI) data is acquired using a 2-D multislice temperature sensitive echo planar imaging sequence collecting five planes of temperature sensitive images every 5 s [19] on a 1.5 T MRI scanner. The cost

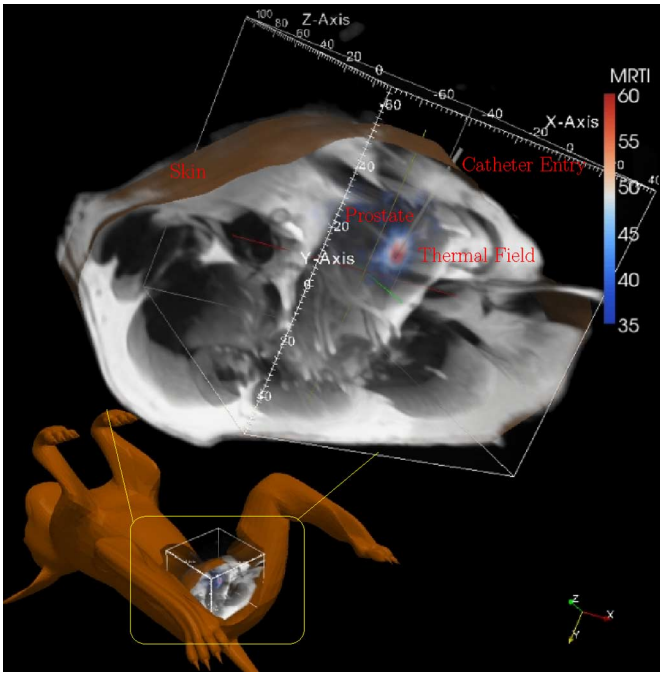

Fig. 1. Schematic diagram of *in vivo* MR-guided LITT calibration procedure in a canine model of prostate. Contrast-enhanced T1-W MR images have been volume rendered to better visualize the relationship of the target volume and applicator trajectory to the surrounding anatomy. As displayed, the subject was stabilized in the supine position with legs upward. A stainless steel stylet was used to insert the laser catheter consisting of a 700 μm core diameter, 1 cm diffusing-tip silica fiber within a 2-mm diameter water-cooled catheter (light gray cylinder). A nondestructive calibration pulse is applied under MR temperature monitoring. A volume rendering of the multiplanar thermal images (in °C) is registered and fused with the 3-D anatomy to visualize the 3-D volume of therapy.

function is then

$$Q(u(\mathbf{x},t)) = \frac{1}{2}\|u(\mathbf{x},t) - u^{\mathrm{MRTI}}(\mathbf{x},t)\|^2_{L^2(\Delta T;L^2(\Omega))} = \frac{1}{2}\int_\Omega \int_{\Delta T} \left(u(\mathbf{x},t) - u^{\mathrm{MRTI}}(\mathbf{x},t)\right)^2 \, dtdx \quad (1)$$

where $dx = dx_1 dx_2 dx_3$ being a volume element and the time interval of interest is denoted by ΔT. The simulation of the time evolution of temperature field within the biological domain is constrained by the classical Pennes model [16] of bioheat transfer with a isotropic laser heat source.

Pennes model has been shown to provide very accurate prediction of bioheat transfer [5], [14], [23] and is used as the basis of the finite element prediction. The full initial boundary value model is defined by the following system:

$$\begin{aligned}
&\rho c_p \frac{\partial u}{\partial t} - \nabla\cdot(k(u,\mathbf{x})\nabla u) \\
&\qquad + \omega(u,\mathbf{x}) c_b (u - u_a) = Q_{\mathrm{laser}}(\mathbf{x},t), \quad [\text{in } \Omega] \\
&Q_{\mathrm{laser}}(\mathbf{x},t) = 3P(t)\mu_a\mu_{tr}\frac{\exp(-\mu_{\mathrm{eff}}\|\mathbf{x}-\mathbf{x}_0\|)}{4\pi\|\mathbf{x}-\mathbf{x}_0\|} \\
&\mu_{tr} = \mu_a + \mu_s(1-g), \qquad \mu_{\mathrm{eff}} = \sqrt{3\mu_a\mu_{tr}} \\
&-k(u,\mathbf{x})\nabla u\cdot\mathbf{n} = \mathcal{G}, \qquad \text{on } \partial\Omega_N \\
&-k(u,\mathbf{x})\nabla u\cdot\mathbf{n} = h(u-u_\infty), \qquad \text{on } \partial\Omega_C. \qquad (2)
\end{aligned}$$

The initial temperature field $u(\mathbf{x},0) = u^0$ is taken as the measured baseline body temperature. The density of the continuum is denoted ρ and the specific heat of blood is denoted $c_b\,[\mathrm{J(kg\cdot K)}^{-1}]$. On the Cauchy boundary $\partial\Omega_C$, h is the coefficient of cooling and u_∞ is the ambient temperature. The prescribed heat flux, on the Neumann boundary $\partial\Omega_N$, is denoted $\mathcal{G}$. The optical-thermal response to the laser source, $Q_{\mathrm{laser}}(\mathbf{x},t)$, is modeled as the classical spherically symmetric isotropic solution to the transport equation of light within a laser-irradiated tissue [22]. $P(t)$ is the laser power as a function of time, μ_a and μ_s are laser coefficients related to laser wavelength and give probability of absorption and scattering of photons, respectively. The anisotropic factor is denoted g and $\mathbf{x}_0$ denotes the position of laser photon source. The scalar-valued coefficient of thermal conductivity is modeled with a nonlinear temperature relation

$$k(u,\mathbf{x}) = k_0(\mathbf{x}) + k_1\ a\tan(k_2(u-k_3))$$

where $k_0(\mathbf{x})[J(\mathrm{s\cdot m\cdot K})^{-1}]$, $k_1[J(\mathrm{s\cdot m\cdot K})^{-1}]$, $k_2[1/\mathrm{K}]$, $k_3\ [K] \in \mathbb{R}$. Perfusion is modeled with a nonlinear dependence on temperature (see Fig. 3)

$$\omega(u,\mathbf{x}) = \omega_0(\mathbf{x}) + \frac{w_N + w_D}{2} + \frac{2}{\pi}\left[\begin{array}{l} \dfrac{w_I - w_N}{2}a\tan(w_2(u-w_{NI})) \\ -\dfrac{w_I - w_D}{2}a\tan(w_2(u-w_{ID})) \end{array}\right]$$

where $\omega_0[\mathrm{kg}/(\mathrm{s\cdot m}^3)]$, $\omega_N[\mathrm{kg}/(\mathrm{s\cdot m}^3)]$, $\omega_I[\mathrm{kg}/(\mathrm{s\cdot m}^3)]$, $\omega_D[\mathrm{kg}/(\mathrm{s\cdot m}^3)], \omega_2\ [1/\mathrm{K}], \omega_{NI}\ [\mathrm{K}], \omega_{ID}\ [\mathrm{K}] \in \mathbb{R}$. The assumed perfusion model is an extension of the constitutive model used in [15] and attempts to recover the observed physiological effects of perfused tissue.

During a thermal therapy, the applied heat begins to dilate the vasculature at a temperature of ω_{NI} and the normal value of the perfusion ω_N increases to a state of hyper perfusion ω_I. Beyond a critical threshold temperature ω_{ID}, the vasculature is damaged and a reduced amount of perfusion is seen, which is denoted by ω_D. In addition to modeling the vasculature breakdown above a temperature threshold, the perfusion model attempts to capture the expected hyper-perfusion under hyperthermia conditions. The linear components of the perfusion, $\omega_0(\mathbf{x})$, and thermal conductivity, $k_0(\mathbf{x})$, are allowed to vary spatially within a local region of interest $r = 1$cm, around the laser source

$$k_0(u,\mathbf{x}) = \begin{cases} k_0,\ x \notin \mathcal{B}_r(\mathbf{x}) \\ k_0(\mathbf{x}),\ x \in \mathcal{B}_r(\mathbf{x}) \end{cases}$$

$$\omega_0(\mathbf{x}) = \begin{cases} \omega_0,\ x \notin \mathcal{B}_r(\mathbf{x}) \\ \omega_0(\mathbf{x}),\ x \in \mathcal{B}_r(\mathbf{x}). \end{cases}$$

Constitutive model data used is summarized in Table I. For the data in this study, the heating is localized to a $\approx$1 cm diameter region about the diffusing interstitial fiber tip and is not significantly influenced by the boundary during delivery. Hence, zero flux boundary conditions are used, $\mathcal{G} = 0$ and $\partial\Omega_C = \emptyset$. The perfusion and thermal conductivities, highlighted in (2), are recovered from the calibration computation. The linear heterogeneous model and the nonlinear constitutive models are

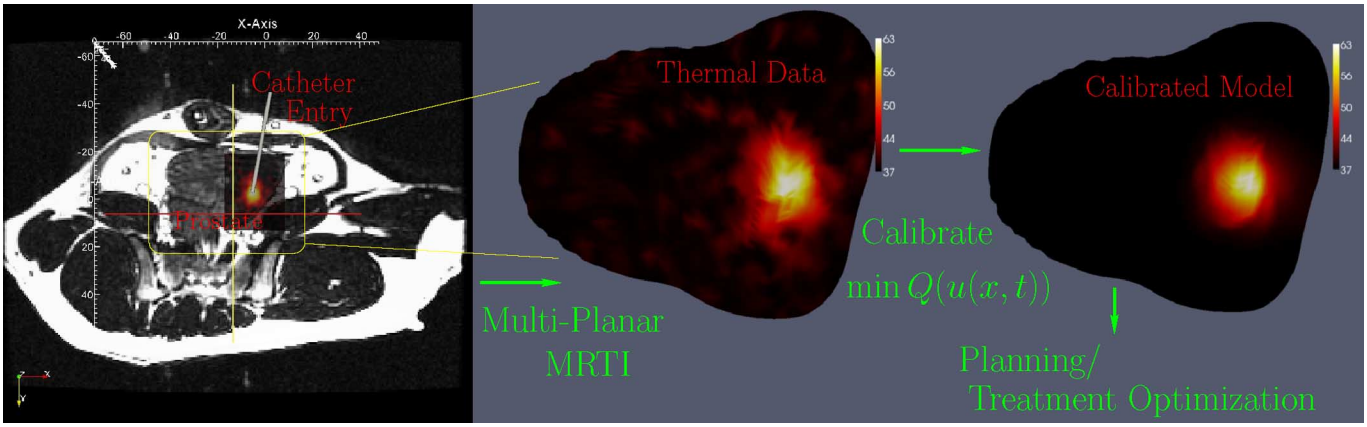

Fig. 2. Schematic diagram of procedure workflow. An axial slice cut from the principle treatment plane demonstrates a 2-D representation of the local heating in that slice. The full field of view shown is 240 mm × 240 mm (scale on image in mm). Multiplanar thermal image data is projected onto a finite element representation of the prostate and used to calibrate a model of the bioheat transfer. The predictive power of the calibrated model may be exploited for further planning and treatment optimization.

TABLE 1
CONSTITUTIVE DATA [8], [22]

g	$\mu_s \ \frac{1}{cm}$	$\mu_a \ \frac{1}{cm}$	$\rho \ \frac{kg}{m^3}$	$u_a \ K$	$c_b \ \frac{J}{kg \cdot K}$	$c_p \ \frac{J}{kg \cdot K}$
0.862	47.0	0.45	1045	308	3840	3600

included in the parameter space explored by the optimization scheme.

We employ a limited-memory variable metric that arises in a quasi-Newton optimization method [3] to drive the calibration problem. Using an adjoint method, the gradient of the objective function (1) with u the solution of (2) can be written as [15]

$$\nabla Q = \begin{bmatrix} -\int_0^T \int_\Omega \frac{\partial k(u)}{\partial k_0} \nabla u \cdot \nabla p \, \hat{k}_0(\mathbf{x}) \, dxdt \\ -\int_0^T \int_\Omega \frac{\partial k(u)}{\partial k_1} \nabla u \cdot \nabla p \, \hat{k}_1 \, dxdt \\ -\int_0^T \int_\Omega \frac{\partial k(u)}{\partial k_2} \nabla u \cdot \nabla p \, \hat{k}_2 \, dxdt \\ -\int_0^T \int_\Omega \frac{\partial k(u)}{\partial k_3} \nabla u \cdot \nabla p \, \hat{k}_3 \, dxdt \\ -\int_0^T \int_\Omega \frac{\partial \omega(u)}{\partial \omega_0} (u - u_a) p \, \hat{\omega}_0(\mathbf{x}) \, dxdt \\ -\int_0^T \int_\Omega \frac{\partial \omega(u)}{\partial \omega_N} (u - u_a) p \, \hat{\omega}_N \, dxdt \\ -\int_0^T \int_\Omega \frac{\partial \omega(u)}{\partial \omega_I} (u - u_a) p \, \hat{\omega}_I \, dxdt \\ -\int_0^T \int_\Omega \frac{\partial \omega(u)}{\partial \omega_D} (u - u_a) p \, \hat{\omega}_D \, dxdt \\ -\int_0^T \int_\Omega \frac{\partial \omega(u)}{\partial \omega_2} (u - u_a) p \, \hat{\omega}_2 \, dxdt \\ -\int_0^T \int_\Omega \frac{\partial \omega(u)}{\partial \omega_{NI}} (u - u_a) p \, \hat{\omega}_{NI} \, dxdt \\ -\int_0^T \int_\Omega \frac{\partial \omega(u)}{\partial \omega_{ID}} (u - u_a) p \, \hat{\omega}_{ID} \, dxdt \end{bmatrix}.$$

Here p is the solution to the adjoint problem and $\hat{k}_0(\mathbf{x})$, $\hat{k}_1$, $\hat{k}_2$, $\hat{k}_3$, $\hat{\omega}_0(\mathbf{x})$, $\hat{\omega}_N$, $\hat{\omega}_I$, $\hat{\omega}_D$, $\hat{\omega}_2$, $\hat{\omega}_{NI}$, $\hat{\omega}_{ID}$ are model parameter test functions.

III. EXPERIMENTAL SETUP

In vivo MR-guided LITT experiments were performed at The University of Texas M.D. Anderson Cancer Center, Houston, Texas. Handling of the canine was in accordance with an Institutional Animal Care and Use Committee approved protocol. General anesthesia was induced utilizing meditomidine (0.5 mg/kg, intramuscular) and 2% isoflurane was used to maintain general anesthesia throughout the duration of the experiment. The experimental configuration for the calibration study is illustrated conceptually in Fig. 1. A finite element method (FEM) mesh of the full prostate anatomy for treatment planning (see Fig. 1) was created using preoperative axial imaging data of the canine prostate and the neighboring anatomy. Two first-order hexahedral meshes were used in the study. The lower resolution mesh consisted of 8817 elements and 9344 nodes and the higher resolution mesh consisted of 22 376 elements and 24 539 nodes. The meshes consisted of 8 and 12 elements across the diameter of the heating region, respectively. An example of the lower mesh resolution is provided in the cutplanes shown in Fig. 4(a).

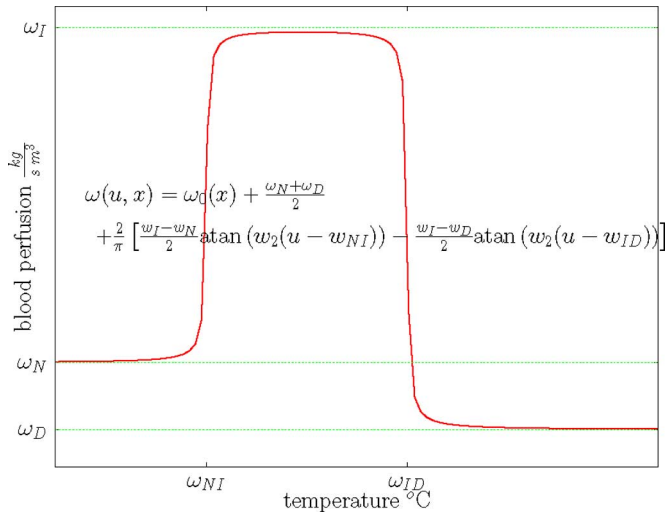

Fig. 3. Nonlinear dependence of perfusion on temperature. As shown $\omega_0(x) = 0$.

Axial and coronal planning images were acquired and used in conjunction with fiducials on a planning template to guide the position of the laser fiber before applying the power. All images were acquired on a clinical 1.5-T MR scanner (Excite HD, GEHT, Waukesha, WI) equipped with high-performance gradients (40 $\text{mT}\cdot\text{m}^{-1}$maximum amplitude and

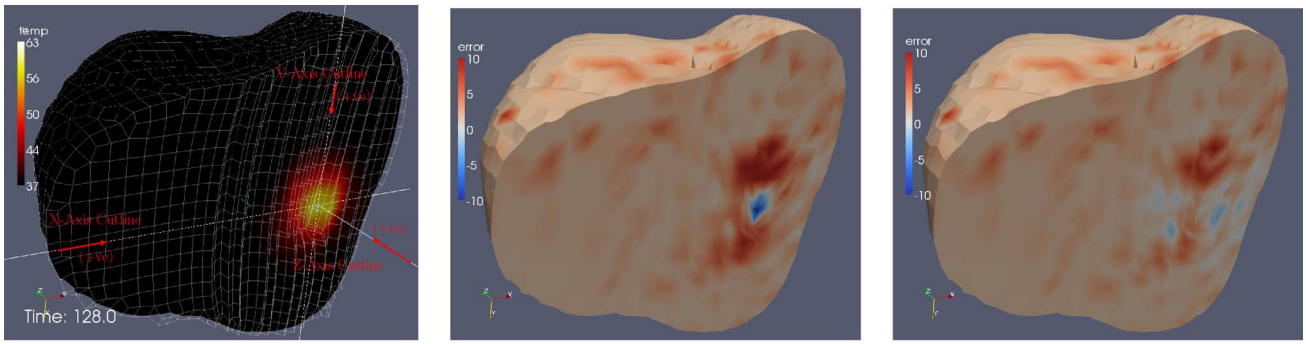

(a) (b) (c)

Fig. 4. (a) Cutplane though the FE prostate model illustrating the postcalibration temperature prediction of Pennes model. The cutplane shown is intersecting and coplanar with the catheter. The temperature is given in (°C). Mesh lines illustrate the mesh resolution. Profiles along the *x*-, *y*-, and *z*-axis are taken with respect to the displayed orientation. The thermal image history along the *y*-axis is shown in Fig. 5(b). The postcalibration error between the predicted temperature and the thermal image temperature along the *x*-axis is shown in Fig. 5. A cutplane through the error field $u - u^{\mathrm{MRTI}}$ is shown in (°C). (b) Precalibration and (c) postcalibration errors for comparison. The plotted error is seen to be significantly reduced postcalibration.

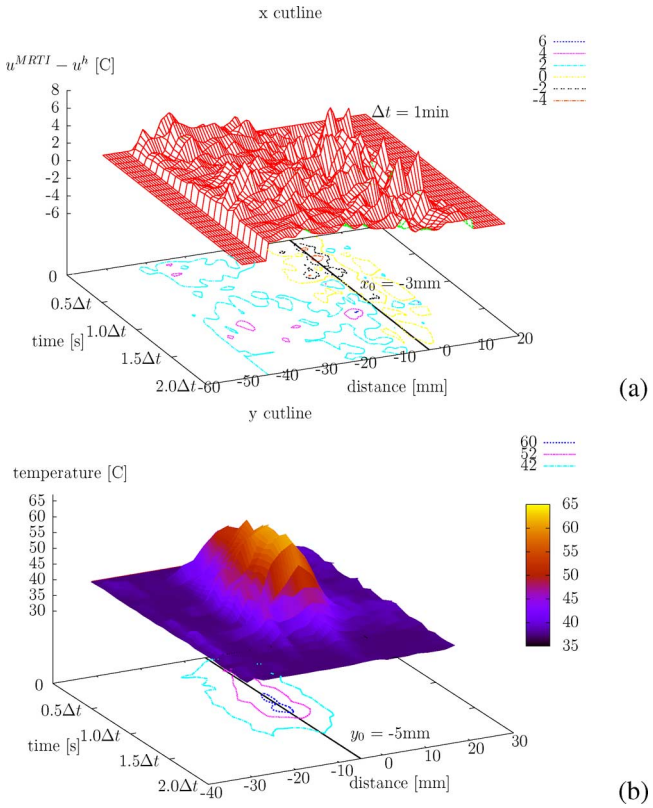

(a) (b)

Fig. 5. Time-varying plots of the postcalibration pointwise error in the model prediction, $u - u^{\mathrm{MRTI}}$, along the *x*-axis of Fig. 4(a) and of the thermal image data along the *y*-axis of Fig. 4(a). The temperature and distance are given in degree Celsius and millimeter, respectively. The units of time are provided with respect to the time duration of the 5 W calibration pulse = 60 s = Δt. Iso-error lines (a) and temperature isotherms (b) are projected onto the time-distance plane. The DICOM coordinate of the laser tip along each cutline $x_0 = -3$ mm and $y_0 = -5$ mm, is labeled as a reference.

$150\ \mathrm{T} \cdot \mathrm{m}^{-1} \cdot \mathrm{s}^{-1}$ maximum slew rate) and fast receiver hardware (bandwidth $\pm$ 500 MHz). A stainless steel stylet was used for inserting the laser catheter, 400 μm core diameter silica fiber in a water-cooled diffused tip catheter (Visualase Inc. Houston, TX). The location of the laser, in DICOM coordinates, was established from the intra-operative images and used in the calibration simulations. A region of the prostate of an anesthetized dog was heated with a nondestructive test pulse from an interstitial laser fiber (980 nm; 5 W for 60 s) housed in an actively cooled applicator $\equiv \Delta t$. The diffusing interstitial laser source is expected to emit a uniform and homogeneous fluence. Real-time multiplanar MRTI based on the temperature dependence of the proton resonance frequency (PRF) [11] monitored the heating and cooling phases of the laser test pulse. The ON/OFF times of the laser were known and controlled by the software so that *a priori* knowledge of beam on and off time was known. The pulse-repetition frequency (PRF) technique uses a complex phase subtraction technique; each consecutive phase image is subtracted from a baseline image that was acquired prior to heating [19]. These phase difference images are proportional to temperature difference Δu. To convert phase to temperature, other factors including echo time (15 ms), water proton resonance frequency (63.87 MHz), and the temperature sensitivity of the water proton (-0.0097 ppm/°C [11]) are required. The image acquisition time of the thermal imaging data in this study is five planes of complex image data every 5 s. In addition to a spatial median-deriche filtering pipeline, a space-time filter was also applied to the thermal imaging data; if the thermal data at a pixel changes by more than 11 °C it is considered noise and filtered. The 11 °C threshold is based on rates of heating observed in previous *in vivo* experiments in conjunction with the *a priori* knowledge that we are acquiring via a low power test pulse.

IV. Results

A calibration study to refine simulation parameters was performed varying the amount of thermal imaging data used in the objective function (1) as a function of the heating pulse time $\Delta t \equiv 60$ s. The performance of the metric chosen for the optimization process was studied in terms of the time window of data used and the effect on the final value of the space time norm between the data and the model prediction over the time window $\Delta T = (0, 2.0\Delta t)$. The metrics considered were the space time norm between the data and the model over five time intervals of interest: $\Delta T = (0, 0.5\Delta t)$, $(0, 1.0\Delta t)$, $(0, 1.5\Delta t)$, $(0, 2.0\Delta t)$, and $(1.0\Delta t, 2.0\Delta t)$. The time intervals $\Delta T = (0, 0.5\Delta t)$ and

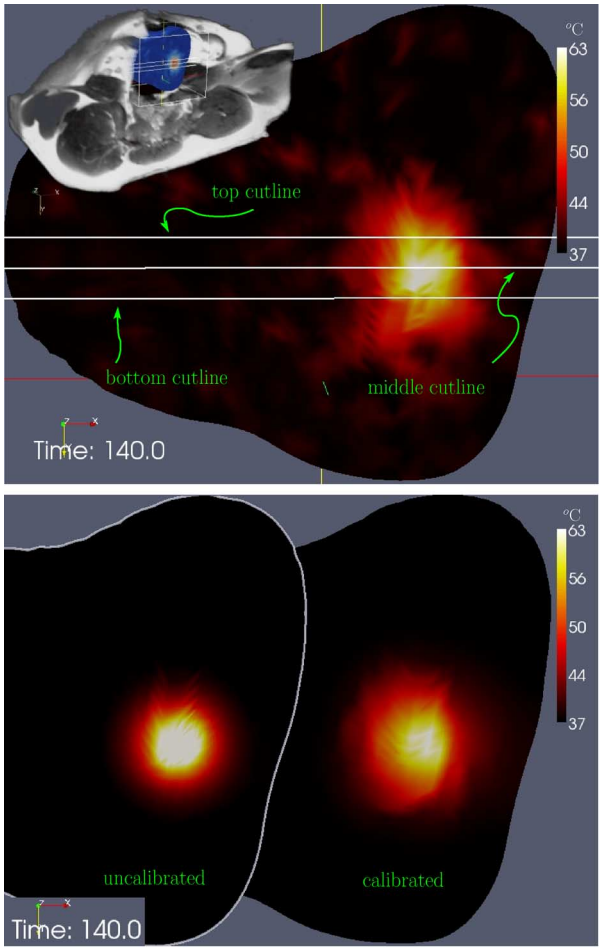

Fig. 6. Comparison of cutplanes through the (a) measured MR temperature image and (b) precalibration and postcalibration calibration finite element prediction is shown. The cutplanes are taken at the same axial position within the anatomy; the plane is 3 mm from the plane that contains the catheter. The temperature scale is shown in (°C). A reference of the axial position is provided in the 3-D insert of (a). At the time instance shown the prostate has been exposed to a dose of 5 W for 55 s, $\approx 0.9\Delta t$. The calibration problem involves recovering the spatially varying thermal properties within a small neighborhood around the laser tip. The illustration shown in (b) represents the inverse problem recovery of $\approx$ 3700 model parameters and allows for the non isotropic heating contours shown. (top, middle, and bottom) Cutlines (a) are used to compare the pointwise thermal image temperature and precalibration and postcalibration finite element prediction of the temperature versus cutline distance Fig. 7.

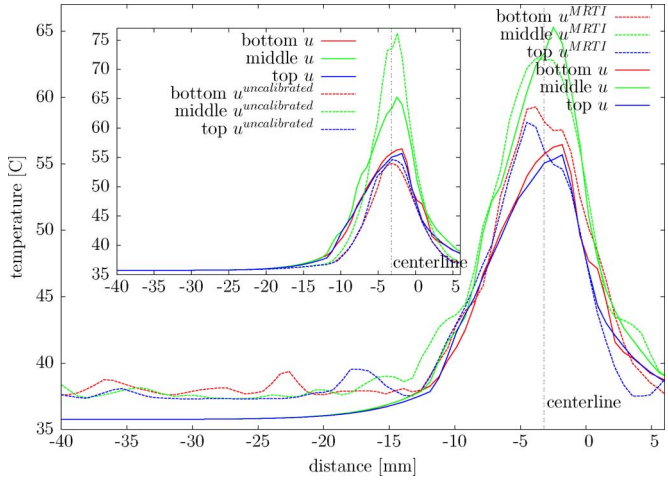

Fig. 7. Cutlines as in Fig. 6(a) are used to compare the pointwise thermal image temperature and precalibration and postcalibration finite element prediction of the temperature versus cutline distance (top, middle, and bottom). The profiles illustrate the effect of the heterogeneity. Uncalibrated, the cutlines are symmetric; calibrated, cutlines demonstrate an asymmetric heating. Graph lines are color-coded to represent the corresponding profile for thermal image and FEM prediction.

$(0, 1.0\Delta t)$ were chosen to study the effect of using only the heating phase for the calibration calculations. The time intervals $\Delta T = (0, 1.5\Delta t)$ and $(0, 2.0\Delta t)$ captures the heating and cooling of the *in vivo* tissue. The time interval $\Delta T = (1.0\Delta t, 0, 2.0\Delta t)$ attempts to eliminate the laser source and isolate the tissue-specific properties from the calibration problem and account only for the cooling of the tissue. Moreover, the behavior of the calibration problem was studied using homogeneous model coefficients versus heterogeneous model coefficients with and without the nonlinearities of the constitutive relationships for the perfusion and thermal conductivity.

A postnonlinear, heterogeneous calibration comparison between the Pennes model and thermal imaging data projected onto the finite element mesh is given in Figs. 4 and 5, respectively. Fig. 4 compares a cutplane that intersects the expected plane of highest heating pre and postcalibration. The heterogeneous tissue property recovery allows for the nonisotropic heating contours observed in the Pennes model prediction [see Fig. 4(a)]. The relative position of the temperature profiles and temperature history (see Fig. 5) are shown in Fig. 4(a). The temperature–time history during the cooling agrees with the exponential decay of the temperature expected from a classical separation of variables solution to the linear heat equation. The calibrated model prediction shows good agreement with the thermal images. The main source of disagreement in the pointwise error [see Figs. 4(a) and 5(a)] can be attributed to noise in the thermal imaging data away from the laser probe. However, the average standard deviation of preheating thermal images measured in a $5 \times 5 \times 5$ pixel ROI within the contralateral lobe of the prostate was 1.53 °C.

The benefit of utilizing spatially heterogeneous techniques for model calibration is shown in Figs. 6 and 7, respectively. Corresponding cutplanes through the uncalibrated model prediction with homogeneous coefficients is compared to the calibrated model prediction with heterogeneous coefficients [see Fig. 6(b)]. The corresponding thermal imaging data is provided for a reference [see Fig. 6(a)]. The model prediction with homogeneous coefficient is seen to create spherical isotherms; this is expected from an isotopic source. Model predictions with heterogeneous coefficients are seen able to recapitulate the structure of the isotherms in the thermal imaging data. This phenomenon is further illustrated in the temperature profiles provided in Fig. 7. Profiles through the homogeneous case are symmetric about the axis of heating as expected, but profiles through the heterogeneous case are asymmetric and better agree with the thermal imaging data.

A comprehensive summary of the calibration study is provided in Fig. 8. The study was done at two discretizations of the geometry, 9344 DOF and 24 539 DOF using linear

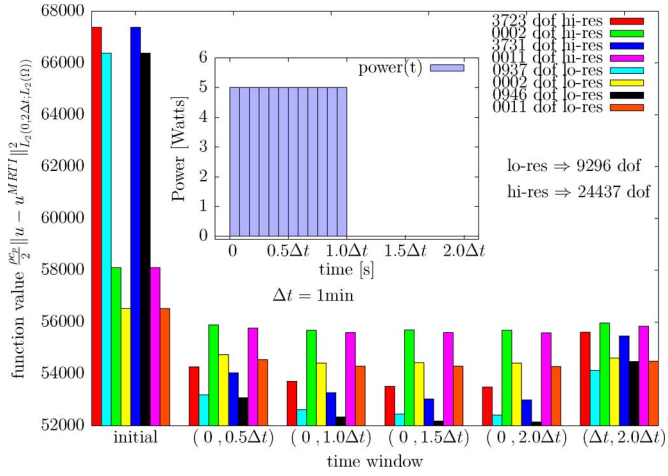

Fig. 8. Summary of a calibration study using various time windows of thermal image information is shown. The power versus time profile of the calibration pulse is shown in the insert; the pulse is held constant at 5 W for $\Delta t = 60$ s and then turned OFF. The study compares the effect of using the $\|\cdot\|^2_{L_2(0,0.5\Delta t;L_2(\Omega))}$, $\|\cdot\|^2_{L_2(0,1.0\Delta t;L_2(\Omega))}$, $\|\cdot\|^2_{L_2(0,1.5\Delta t;L_2(\Omega))}$, $\|\cdot\|^2_{L_2(0,2.0\Delta t;L_2(\Omega))}$, $\|\cdot\|^2_{L_2(\Delta t,2.0\Delta t;L_2(\Omega))}$ norms for the calibration problem. The metric of the comparison is the full space–time norm $\|\cdot\|^2_{L_2(0,2\Delta t;L_2(\Omega))}$ of the difference between the thermal image data and the finite element comparison. The initial preoptimization value of the objective function is provided as a reference for the relative decrease. Different initial thermal conductivity and perfusion distributions for the heterogeneous and homogeneous solve account for the initial discrepancy in the objective function. The plot demonstrates that the optimal amount of thermal image information to use in the calibration problem is 1.5× pulse duration. This suggests that the calibration process can be implemented in near real-time with minimal impact on latency in the feedback control paradigm.

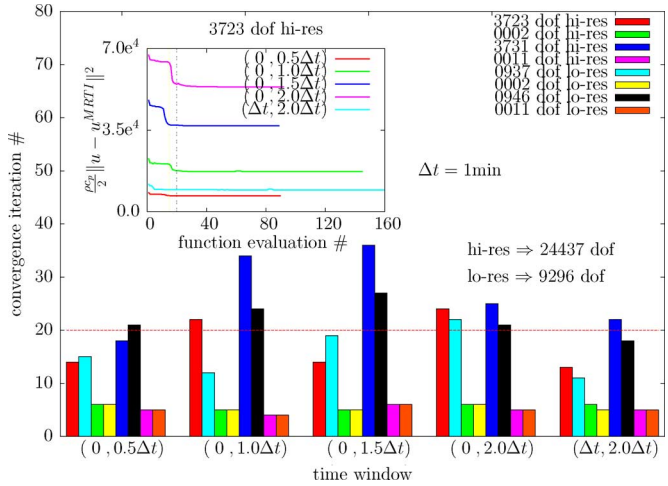

Fig. 9. Number of function evaluations required for convergence of the quasi-Newton optimization method used in the calibration study is shown. The graph is intended to convey the general convergence behavior observed from the breadth of the calibration problems studied. The PDE constrained optimization problems are seen to have converged to their minimum within an average of 20 function evaluations. This data can be used to estimate the time required for a real-time calibration. Surgery protocols should allow time to complete 20 function-gradient computations for the calibration phase. The objective function values as a function of iteration number is shown in the insert to illustrate the typical convergence behavior observed.

homogeneous model coefficients, nonlinear homogeneous coefficients, heterogeneous linear coefficients, and heterogeneous nonlinear coefficients. The linear homogeneous, nonlinear homogeneous, heterogeneous linear, and heterogeneous nonlinear cases resulted in 2/2 DOF, 11/11 DOF, 937/3723 DOF, and 946/3731 DOF for the optimization problem; respectively, at the two model discretizations studied. The space–time norm over the entirety of the data was used as the basis for comparison, i.e., for $\Delta T = (0, 0.5\Delta t)$ the model was calibrated using the $\|\cdot\|^2_{L_2(0,0.5\Delta t;L_2(\Omega))}$ objective function and then propagated over the entire time interval $\Delta T = (0, 2.0\Delta t)$ as a metric for comparison against other data time intervals. The initial precalibration value of the objective function is provided as a reference. Results indicate that using a data interval $\Delta T = (0, 1.5\Delta t)$ for the calibration problem provides the greatest objective function decrease for the least amount of computational work and is thus optimal in terms of computation efficiently. The benefit for using the heterogeneous calibration over the homogeneous calibration is clearly in the difference of the magnitude of the objective function (1), however, the benefit of the constitutive nonlinearities is not as dramatic.

The observed objective function convergence history for selected calibration problems is presented in Fig. 9. The graph is intended to convey the *general convergence behavior* of the breadth of the calibration problems studied. The number function evaluations required for convergence of the calibration problem for homogeneous and heterogeneous models coefficients with and without constitutive nonlinearities is shown for the $(0, 0.5\Delta t)$, $(0, 1.0\Delta t)$, $(0, 1.5\Delta t)$, $(0, 2.0\Delta t)$, and $(1.0\Delta t, 2.0\Delta t)$ time windows. The insert of Fig. 9 shows the convergence trend of the optimizer for the linear homogeneous case with heterogeneous model coefficients at the highest resolution considered in this study. The two significant decreases in the objective function seen in Fig. 9 were typically associated first with a large change in the thermal conductivity followed by a change in the perfusion. On average, the optimizer is seen to have converged by twenty function-gradient computations. As observed in the insert of Fig. 9, the calibration problem appears to converge well before the typical relative and absolute value optimization convergence metrics are reached. The metric used to report the convergence in Fig. 9 was weakened to a form (3) that retrospectively looks at the history and uses the relative difference between the absolute minimum-*overconverged* function value obtained Q_{minimum} and the starting value Q_{initial}

$$\frac{Q_{\text{initial}} - Q_{\text{converged}}}{Q_{\text{initial}} - Q_{\text{minimum}}} < 1.5\%. \tag{3}$$

For a particular problem, when $Q_{\text{converged}}$ satisfies (3), convergence is reached. Results provide an estimate that the lower bound wall clock time needed for a real-time patient-specific calibration computation is 3 min (for this particular study); 90 s worth of simulation for a function-gradient computation takes 9 s [9], multiplied by twenty objective function-gradient computations needed for convergence.

V. Discussion and Conclusion

Calibration of the model based on accounting for spatial heterogeneities in the tissue produce much greater improvements in

predicted temperature than upgrading terms in nonlinear constitutive equations assuming homogeneous tissue. This suggests an effective constitutive alternative to modeling the nonlinear bioheat transfer observed in soft tissue. In light of the fact that this study was limited to homogeneous constitutive nonlinearities, the benefit of allowing for a spatially varying constitutive nonlinearity in the calibration is not clear. Linear model heterogeneities provide a dramatic increase in the model prediction. The possible relative increase in model accuracy obtained by adding spatially varying constitutive nonlinearities does not seem to be worth the cost of implementation. The tissue behaves as a heterogeneous but linearly conductive media.

The thermal source in this study was modeled as isotropic. As illustrated by the agreement in the model prediction (see Fig. 6) the modeling error in the laser source appears to have been compensated by the spatially varying thermal parameter field. Further work is needed to differentiate the extent of effects of the actual tissue heterogeneity, the photon distribution emitted from the laser, and the cooling systems typically accompanying laser applicators. Preliminary computations of the effect of the laser fiber active cooling system have shown substantial effects on the resulting thermal distribution.

In summary, results demonstrate that a calibration pulse prior to MRgLITT can be used to substantially increase modeling accuracy for delivery prediction. Further, results indicate the existence of a critical time interval of the calibration objective function beyond which further use of data provides diminishing returns. This observation combined with the relatively limited amount of function-gradient computations needed for convergence (see Fig. 9) provides an achievable strict upper bound on the computational time needed to converge to a calibrated Pennes model; this may be used as a reference for computer guided MRgLITT protocol design. However, within the perspective of a clinical setting, the overhead associated with the computation of the calibration problem needs an order of magnitude speedup. Significant algorithmic changes are needed to achieve this level of performance. One possible method, that is even more suitable for dynamic feedback, is suggested by the presented data. The smaller time windows *did* decrease the objective function, even though not dramatically. These relatively computationally inexpensive problems may be used as initial conditions for the full calibration problems of interest and the overhead of implementing the necessary complex data structures would be beneficial. We hope that these results help guide independent *in vivo* experiments and translational research on the path to realizing the model calibration aspect of computer guided LITT technology within a clinical setting.

ACKNOWLEDGMENT

The authors would like to thank the Insight Segmentation and Registration Toolkit (ITK) [12], Paraview [10], Portable Extensible Toolkit for Scientific Computation (PETSc) [2], TAO [3], libMesh [13], and CUBIT [20] communities for providing truly enabling software for scientific computation and visualization. The initial 3-D canine model in Fig. 1 was provided by AddZero and obtained from the official Blender [17] model repository.

REFERENCES

[1] D. E. Atkins, K. K. Droegemeier, S. I. Feldman, H. Garcia-Molina, M. L. Klein, D. G. Messerschmitt, P. Messina, J. P. Ostriker, and M. H. Wright, "Revolutionizing science and engineering through cyberinfrastructure," *Rep. Nat. Sci. Foundation Blue-Ribbon Advisory Panel on Cyberinfrastructure*, 2003.

[2] S. Balay, W. D. Gropp, L. C. McInnes, and B. F. Smith, "Petsc users manual," Argonne National Laboratory, Tech. Rep. ANL-95/11—Revision 2.1.5, 2003.

[3] S. J. Benson, L. C. McInnes, J. Moré, and J. Sarich. (2005). "TAO user manual (revision 1.8)," Mathematics and Computer Science Division, Argonne National Laboratory, Tech. Rep. ANL/MCS-TM-242, [Online]. Available: http://www.mcs.anl.gov/tao

[4] A. Carpentier, R. J. McNichols, R. J. Stafford, J. Itzcovitz, J. P. Guichard, D. Reizine, S. Delaloge, E. Vicaut, D. Payen, A. Gowda *et al.*, "Real-time magnetic resonance-guided laser thermal therapy for focal metastatic brain tumors," *Neurosurgery*, vol. 63, no. 1(Suppl. 1), pp. 21–29, 2008.

[5] C. K. Charny, "Mathematical models of bioheat transfer," *Adv. Heat Trans.*, vol. 22, pp. 19–155, 1992.

[6] F. Darema. (2006). DDDAS: Dynamic data driven applications systems. [Online]. Available: www.nsf.gov/cise/cns/dddas

[7] K. R. Diller, J. T. Oden, C. Bajaj, J. C. Browne, J. Hazle, I. Babuška, J. Bass, L. Bidaut, L. Demkowicz, A. Elliott, Y. Feng, D. Fuentes, S. Goswami, A. Hawkins, S. Khoshnevis, B. Kwon, S. Prudhomme, and R. J. Stafford, "Computational infrastructure for the real-time patient-specific treatment of cancer," in *Advances in Numerical Heat Transfer*, Numerical Implementation of Bioheat Models and Equations, vol. 3. New York, Taylor & Francis, 2008, ch. 9.

[8] K. R. Diller, J. W. Valvano, and J. A. Pearce, "Bioheat transfer," in *The CRC Handbook of Mech. Engr.*, F. Kreith and Goswami, Eds. 2nd ed. Boca Raton, FL: CRC Press, 2005, pp. 4-278–4-357.

[9] D. Fuentes, J. T. Oden, K. R. Diller, J. Hazle, A. Elliott, A. Shetty, and R. J. Stafford, "Computational modeling and real-time control of patient-specific laser treatment cancer," *Ann. BME.*, vol. 37, no. 4, pp. 763–782, 2009.

[10] A. Henderson and J. Ahrens, *The ParaView Guide*. Clifton Park, NY: Kitware, Inc., 2004.

[11] J. C. Hindman, "Proton resonance shift of water in the gas and liquid states," *J. Chem. Phys.*, vol. 44, pp. 4582–4592, 1966.

[12] L. Ibanez, W. Schroeder, L. Ng, and J. Cates. (2005). The ITK Software Guide, 2nd ed. Clifton Park, NY: Kitware, Inc., ISBN 1-930934-15-7, [Online]. Available: http://www.itk.org/ItkSoftwareGuide.pdf

[13] B. S. Kirk and J. W. Peterson. (2003). libMesh-a C++ Finite Element Library, CFDLab. Available: http://libmesh.sourceforge.net

[14] J. Liu, L. Zhu, and L. Xu, "Studies on the three-dimensional temperature transients in the canine prostate during transurethral microwave thermal therapy," *J. Biomech. Eng.*, vol. 122, pp. 372–378, 2000.

[15] J. T. Oden, K. R. Diller, C. Bajaj, J. C. Browne, J. Hazle, I. Babuška, J. Bass, L. Demkowicz, Y. Feng, D. Fuentes, S. Prudhomme, M. N. Rylander, R. J. Stafford, and Y. Zhang, "Dynamic data-driven finite element models for laser treatment of prostate cancer," *Num. Meth. PDE*, vol. 23, no. 4, pp. 904–922, 2007.

[16] H. H. Pennes, "Analysis of tissue and arterial blood temperatures in the resting forearm," *J. Appl. Physiol.*, vol. 1, pp. 93–122, 1948.

[17] T. Roosendaal and C. Wartmann, *The official Blender 2.0 Guide*. Kenansville, NC: Primatech, 2000.

[18] R. Salomir, F. C. Vimeux, J. A. de Zwart, N. Grenier, and C. T. Moonen, "Hyperthermia by MR-guided focused ultrasound: Accurate temperature control based on fast MRI and a physical model of local energy deposition and heat conduction," *Magn. Reson. Med.*, vol. 43, no. 3, pp. 342–347, 2000.

[19] R. J. Stafford, R. E. Price, C. J. Diederich, M. Kangasniemi, L. E. Olsson, and J. D. Hazle, "Interleaved echo-planar imaging for fast multiplanar magnetic resonance temperature imaging of ultrasound thermal ablation therapy," *J. Magn. Reson. Imag.*, vol. 20, no. 4, pp. 706–714, 2004.

[20] T. Blacker *et al.* (2008). "Cubit Users Manual," [Online]. Available: http://cubit.sandia.gov/documentation

[21] F. C. Vimeux *et al.* (2008), "Real-time control of focused ultrasound heating based on rapid MR thermometry," *Invest. Radiol.*, vol. 34, no. 3, pp. 190–193, 1999.

[22] A. J. Welch and M. J. C. van Gemert, *Optical-Thermal Response of Laser Irradiated Tissue*. New York: Plenum, 1995.

[23] E. H. Wissler, "Pennes' 1948 paper revisited," *J. Appl. Physiol.*, vol. 85, pp. 35–41, 1998.